Materials Science in Additive Manufacturing

ORIGINAL RESEARCH ARTICLE

Preparation of polyamide 6 and its titanium dioxide photocatalytic composite powders for laser powder bed fusion

Peng Chen[1], Zhaoqing Li[1], Sheng Liu[1], Jin Su[1], Haoze Wang[1], Lei Yang[2], Chunze Yan[1]*, Yusheng Shi[1]

[1]State Key Laboratory of Materials Processing and Die and Mould Technology, School of Materials Science and Engineering, Huazhong University of Science and Technology, Wuhan, China

[2]School of Logistics Engineering, Wuhan University of Technology, Wuhan, China

Abstract

Laser powder bed fusion (LPBF) additive manufacturing is an effective method to prepare three-dimensional ordered network titanium dioxide (TiO_2) photocatalytic materials, therefore enhancing the absorption intensity of incident light and improving the photocatalytic efficiency. However, TiO_2 is difficult to be directly sintered by LPBF due to the high melting point and brittleness. In this study, we prepared a polyamide 6 (PA6)-coated TiO_2 photocatalytic composite powder for LPBF based on the dissolution precipitation polymer coating (DPPC) method and evaluated its LPBF processability. In the precipitation process of PA6, there was a significant crystallization exotherm with temperature recovery. Effective temperature control of this precipitation process had a significant effect on the morphology and particle size distribution of the precipitated powder. The increase of the dissolved concentration of PA6 to 150 g/L produced an obvious temperature gradient of the reactor, resulting in a wide particle size distribution and a powder with a characteristic porous surface. The prepared PA6/TiO_2 composite powder presents a near-spherical porous-surfaced morphology, a high specific surface area of 240.5 m^2/kg, an appropriate Dv(50) of 48.8 μm, and a wide sintering window of 26.6℃, indicating a good LPBF processability and potential of the photocatalytic application.

Keywords: Additive manufacturing; Laser powder bed fusion; Photocatalytic material; Polyamide 6; Titanium dioxide

***Corresponding author:**
Chunze Yan
(c_yan@hust.edu.cn)

Citation: Chen P, Li Z, Liu S, *et al.*, 2022, Preparation of polyamide 6 and its titanium dioxide photocatalytic composite powders for laser powder bed fusion. *Mater Sci Add Manuf.* 1(3): 14.
https://doi.org/10.18063/msam.v1i3.14

Received: July 6, 2022

Accepted: August 9, 2022

Published Online: August 24, 2022

1. Introduction

Titanium dioxide (TiO_2) photocatalytic materials have the advantages of stable chemical properties, good photoelectric characteristics, high catalytic activity, and good accessibility[1,2]. These advantages promote their widespread use in the photocatalytic degradation of environmental pollutants, self-cleaning, solar cells, and photolysis of water for hydrogen production, thus facilitating their broad applications in energy, environmental protection, and medical health fields[3-6]. However, TiO_2 has the problems of the low utilization rate of sunlight and low catalytic efficiency. The electrons in excited state and holes can be easily combined, resulting in low photocatalytic reaction efficiency

of most photocarriers. This greatly limits the practical application range of TiO_2 in research and production[5].

From the perspective of material modification, different methods have been studied to improve the photocatalytic performance of TiO_2, such as semiconductor compounding, dye sensitization, noble metal deposition, and carbon (C) compound modification[7-10]. Among these methods, the research on C-modified TiO_2 is particularly attractive. C-TiO_2 composite can increase the specific surface area of the material, which is conducive to the adsorption of reactive species and the occurrence of catalytic reactions. The composite of C-TiO_2 can also make the photogenerated carrier electrons transfer to C and reduce the recombination of photogenerated electrons and photogenerated hole pairs, thereby improving the catalytic efficiency.

From the perspective of structural design, the researchers proposed to prepare a porous TiO_2 photocatalytic material to provide a three-dimensional (3D) network structure with a large specific surface area, which is beneficial to improve the photocatalytic efficiency and also provides a way for the rapid transfer of photogenerated electrons and holes to reduce their recombination probability[11]. Furthermore, the 3D porous structure is beneficial to generate light scattering channels and enhance the absorption of incident light. At present, the preparation of 3D TiO_2 structure mainly adopts ionic liquid, nickel foam, and template methods[12-14]. The prepared 3D porous photocatalytic materials usually have disordered structures, unavoidable structural defects, and poor experimental repeatability, which are the main limitations restricting their applications[15].

Laser powder bed fusion (LPBF) additive manufacturing is an effective technique for fabricating 3D ordered porous photocatalytic materials[6,16-19], which provides a new idea for solving the problems existing in traditional TiO_2 photocatalytic materials. LPBF also provides an effective technical means for the preparation of ordered porous structures with controllable and repeatable photocatalytic properties[20-22]. Although additive manufacturing has significant advantages in the fabrication of complex ordered structures, its application in the field of photocatalysis is very limited. In this paper, a new polyamide 6 (PA6)-coated TiO_2 composite porous material is prepared for LPBF using the dissolution precipitation polymer coating (DPPC) method. As a polymer material, PA6 provides a carbon source for the carbonization preparation of C-TiO_2 porous photocatalytic material. Carbon-complexed porous TiO_2 can increase the efficiency of photogenerated carrier separation and thus improve the photocatalytic efficiency. However, the DPPC method for PA6 and its TiO_2 composite powders has not been studied in-depth. How to regulate the DPPC process parameters, control the porous morphology and size distribution of precipitated powders, and prepare PA6/TiO_2 composite porous powders suitable for LPBF warrants some in-depth investigations.

2. Experimental section

2.1. Materials preparation

Commercial PA6 granules with the trade name Zytel 7331J were obtained from Dupont, USA. P25 type TiO_2 was a highly dispersed gas phase nanoparticle produced by Degussa Company in Germany. The reaction kettle with the capacity of 10 L was used for DPPC powder preparation (Figure 1A), which mainly includes the reaction unit and its temperature control unit. The schematic of the DPPC method is shown in Figure 1B. First, the reaction kettle was heated to 150°C for 2 h to ensure that the PA6 granules were completely dissolved in a high-temperature and high-pressure alcohol solvent. Afterward, the solution was cooled, and the cooling conditions were controlled so that the PA6 macromolecules were uniformly precipitated to realize the nucleation and the coating of TiO_2. The stirring speed was 300 rpm. Finally, the reactor was cooled to room temperature. After discharge, vacuum filtration, drying, and ball milling, the powder materials can be obtained.

2.2. Characterization

The powder morphology and element mapping were carried out by environmental scanning electron microscope (ESEM, FEI Instrument, Netherlands), electron probe microanalyzer 8050 g, SHIMADZU, Japan, and WDS. The specimens were vacuum-coated with platinum for 300 s to avoid charging. The morphology and crystalline structure of nano-TiO_2 were analyzed by field emission transmission electron microscope (TEM, Talos F200X, FEI Instrument, Netherlands) using high resolution TEM (HRTEM) and selected area electron diffraction modes. The particle size distributions of PA6 and composites powers were tested on Mastersizer 3000 (British Malvern). The angle of repose was tested according to the standard ASTM C 1444-00. Four groups of experiments were performed for each kind of powder, and the diameter of each group was recorded 4 times and the mean value was taken. The AOR was calculated using the following equation:

$$\varphi = \arctan 2h/D_a \quad (1)$$

Where ϕ represents AOR, h is the vertical distance between the top height formed by powder accumulation and the bottom end of the funnel (38.1 mm in this experiment), and D_a is the average value of powder packing diameter obtained after four groups multiplied by 4 measurements of each powder. The measurement of powder bulk density

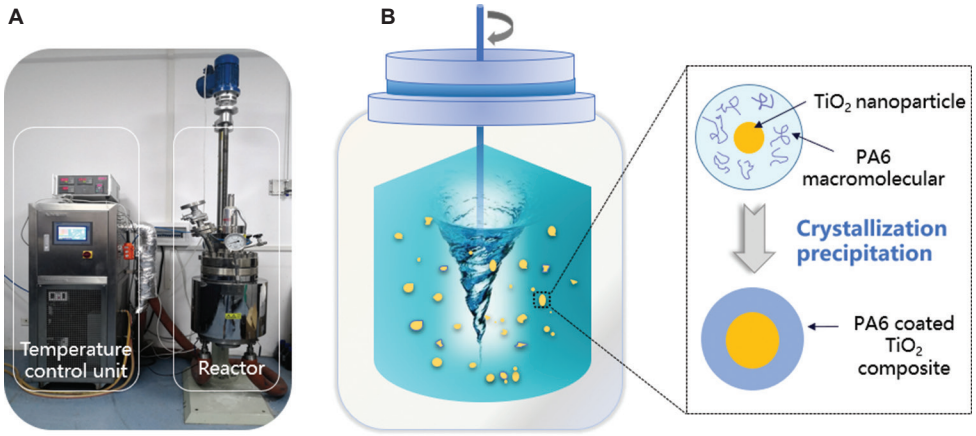

Figure 1. (A) Reaction kettle system. (B) Schematic diagram of DPPC method for the preparation of PA6/TiO_2 composite powders.

was carried out according to the standard ASTM D7481-18. A metal measuring cylinder was placed under the funnel to receive powder quantitatively. The volume of the measuring cylinder was 100 mL. Thermal experiments were performed by Diamond differential scanning calorimetry (DSC, PerkinElmer Instruments, USA) to analyze the melting/crystallization properties of composite powders. The DSC testing was carried out under a nitrogen atmosphere at a heating and cooling rate of 10°C/min. The variation of the crystalline structure was tested on an X'pert3 powder X-ray diffractometer (PANalytical B.V., Netherlands) using Cu Kα radiation at a scan speed of 3°/min.

3. Results and discussion

3.1. Control of precipitation cooling process

First, the precipitation process of PA6 was studied. The precipitation cooling process had an important effect on the morphology and particle size distribution of powders. Figure 2 shows the morphology difference between powder precipitated by rapid cooling at 120°C/h and natural slow cooling at 20°C/h. The powders precipitated by rapid cooling were mainly solid particles, but many of them were featured by incompletely grown sheets. By contrast, the slow-cooling particles stuck with each other. The porous structure of the particle surface is beneficial to the improvement of light absorption efficiency[23,24]. The cooling of the reaction kettle directly determines the particle morphology, size, and surface quality. In the whole cooling process, the control of the precipitation stage plays a key role in the powder properties. Therefore, the whole cooling process was monitored, and the precipitation temperature holding method was adopted to analyze the variation of powder properties.

Figure 3 shows the cooling curve when the reaction kettle was kept at 125°C immediately after precipitation.

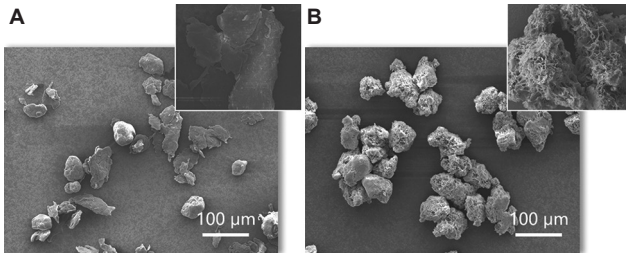

Figure 2. Morphological characteristics of PA6 powders precipitated by (A) rapid cooling at 120°C/h and (B) natural cooling at 20°C/h. The dissolved concentration of PA6 is 50 g/L.

It is obvious that the temperature recovery of PA6 solution occurred in the cooling process, and the dynamic temperature fluctuation occurred in the temperature holding process. This is mainly due to the crystallization exotherm generated during the precipitation of PA6, which increases the temperature of the system. Therefore, the crystallization precipitation temperature of PA6 can be determined according to the transition of the temperature curve. Figure 3 shows that the starting temperature of crystallization precipitation was 124°C. The cooling rate before precipitation was 24.4°C/h, while the cooling rate after precipitation significantly decreased to 16.8°C/h. The exothermic enthalpy during crystallization precipitation increased the temperature of the whole system by 1.8°C, indicating the large exothermic heat from crystallization. Meanwhile, the final steady-state temperature was 0.2°C higher than the equilibrium temperature of 125°C due to the existence of crystallization exothermic enthalpy.

The typical morphology and particle size distribution of powders precipitated at 125°C were studied. It is shown in Figure 4A that the morphology of the powder was nearly spherical. Most of the particles were solid structures without obvious pores, indicating the high solid density of powders. The analysis of particle size distribution

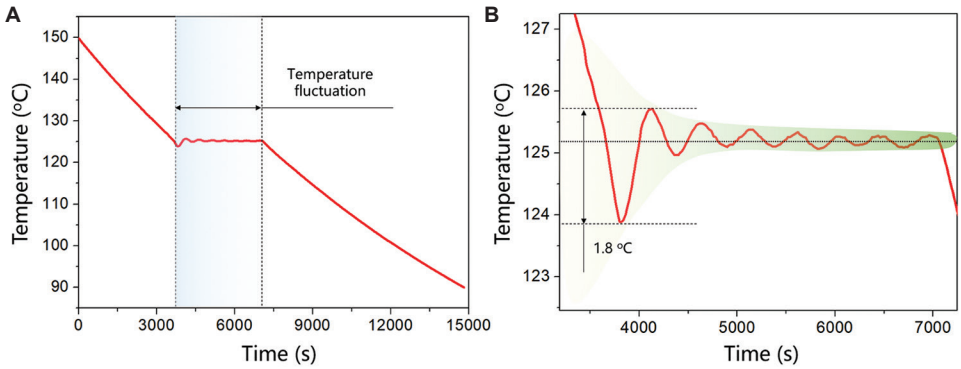

Figure 3. (A) The cooling curve of the reaction kettle held at 125°C for 1 h immediately after precipitation and (B) its characteristic temperature fluctuation. The dissolved concentration of PA6 is 50 g/L.

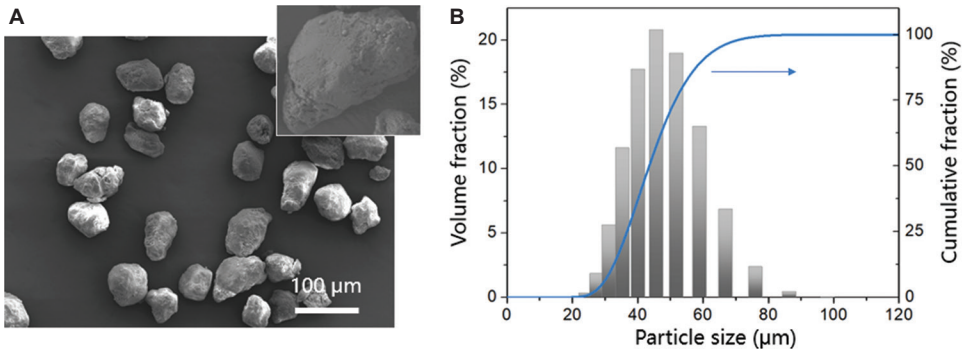

Figure 4. (A) The morphology and (B) particle size distribution of PA6 powders precipitated after holding at 125°C for 1 h. The dissolved concentration of PA6 is 50 g/L.

(Figure 4B) shows that most powders were distributed in the particle size range of 20–90 μm and showed a normal distribution peak at 49.3 μm.

According to the crystallization precipitation temperature and the steady-state temperature, different holding temperatures were taken to study their effects on the powder morphology and particle size distribution (Figures 5 and 6). The changes in powder size at different holding temperatures are shown in Table 1. According to Figure 5, there were distinctly different morphological features of powders precipitated above and below the precipitation temperature. When the holding temperature was low at 120°C, there were many small particles among the powders. The large particles also had an obvious cracking phenomenon, and there were opening pores inside. The particle size showed a bimodal normal distribution, and the small particle powder was aggregated at 10 μm (Figure 6). This is mainly because the particles have already nucleated at 120°C but have not grown up. The temperature holding at this time increased the quantity of small-sized powders. The powders precipitated at 122.5°C showed the morphology transformation of flakes and long strips, and the powder

Table 1. Changes in powder size at different holding temperatures

Parameters	Holding temperature				
	120°C	122.5°C	125°C	127.5°C	130°C
D_v (10)/μm	28.8	29.8	36.2	33.1	25.0
D_v (50)/μm	49.5	45.3	49.3	48.6	40.2
D_v (90)/μm	78.3	68.4	66.7	70.7	63.8
D[3, 2]/μm	41.6	43.1	48.0	46.5	37.6

growth was irregular. Most of the powders showed solid structures, and there was no aggregation of small particles. When the holding temperature was higher than the precipitation temperature at 127.5°C, some powders showed a fish-scale surface, which promotes the formation of internal lapped pores. This is not conducive to powder spreading and density improvement[24]. When the temperature reached 130°C, the excessively high temperature promotes the generation of new secondary nucleated particles with the feature of fish-scale surface. From the perspective of particle size, too high or too low holding temperature can produce small-sized particles.

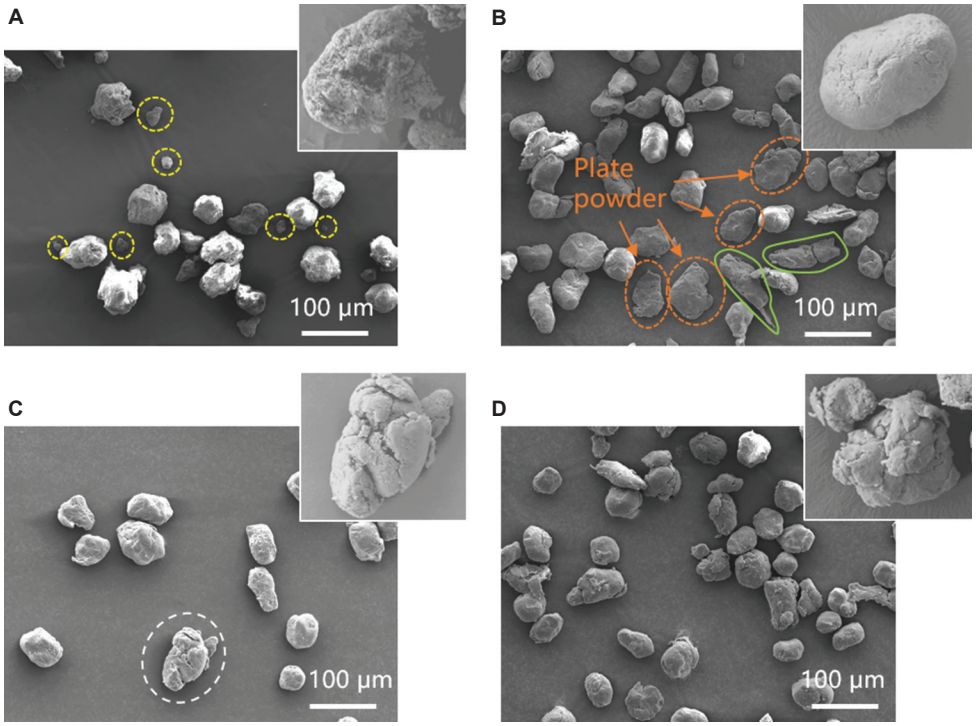

Figure 5. Morphologies of PA6 powders precipitated at different holding temperatures: (A) 120°C, (B) 122.5°C, (C) 127.5°C, and (D) 130°C.

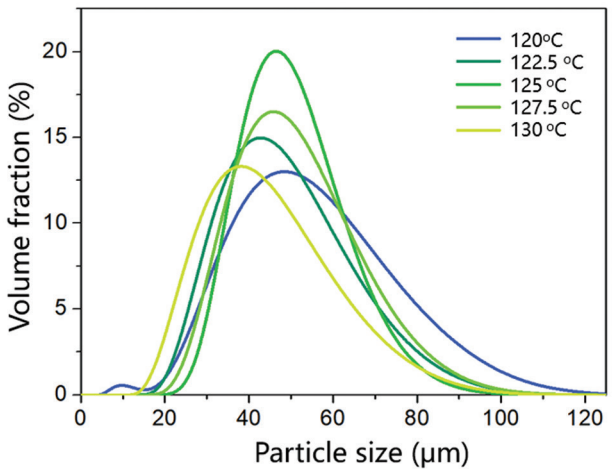

Figure 6. Particle size distributions of PA6 powders precipitated at different holding temperatures.

The small-sized particles from low holding temperatures are caused by an incomplete particle growth process after nucleation, while those from high holding temperatures are caused by secondary nucleation with additional adhesion of surface substances. The heat preservation near the precipitation temperature of 125°C can form particles with a narrow particle size distribution, a uniform particle size, and a smooth surface particle, which is beneficial to the HT-LPBF process.

3.2. Effects of dissolved concentration on powder properties

When the powder was prepared in large quantities, the dissolved concentration of PA6 increased, resulting in a huge difference in particle morphology. Figure 7 shows the changes in morphologies under the concentration conditions of 100 g/L, 150 g/L, and 200 g/L. When the concentration was increased to 100 g/L, the powder surface became rough and uneven, accompanied by the generation of small particles. The powder under the concentration of 150 g/L gradually acquired a porous surface. When the concentration reached 200 g/L, obvious characteristics of multiphase nucleation could be observed. A single particle was formed by the agglomeration of small particles. There was a large number of network structures between the particles, indicating that the particles have already adhered to each other before they grew up.

From a comprehensive analysis, the increase in dissolved concentration leads to the emergence of contradictory phenomena. On the one hand, porous-surfaced powders and rod-like powders were produced. The rod-like powders and porous-surfaced powders appeared only after slow cooling and long-term heat preservation, indicating that the increase in concentration has the same effect as the long-term heat preservation. On the other hand, the agglomeration and inter-bonding of small particles occurred, which are similar to the small particles

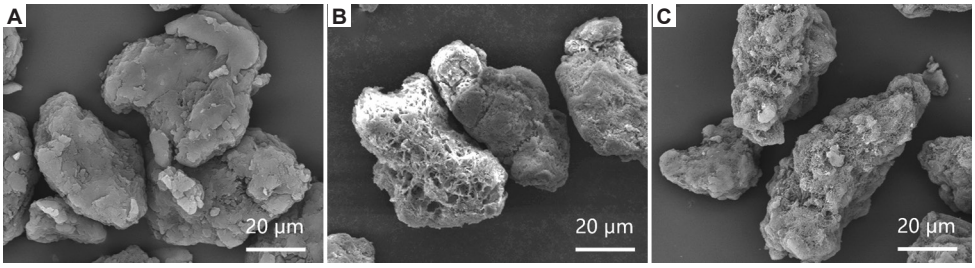

Figure 7. Morphologic difference of powders prepared with different PA6 concentrations: (A) 100 g/L, (B) 150 g/L, and (C) 200 g/L.

produced from low-temperature partial nucleation and high-temperature secondary nucleation. These two aspects indicate that the increase in concentration leads to obvious low-temperature and high-temperature regions, corresponding to the temperature gradient from the kettle wall to the inside of the solution. Therefore, an increase in concentration is not advantageous for uniform precipitation of powders, because the improvement of concentration leads to an increase in the number of nucleation per unit volume and a decrease in the heat transfer rate from the reactor wall to the interior of the solution.

Even so, increasing the concentration would widen the particle size distribution, making it more suitable for increasing the packing density of the LPBF powder bed. The porous-surfaced powders were also favorable for improving photocatalytic performance because a large specific surface area could enhance the absorption of incident light. Based on the concentration of 150 g/L and the condition of 125°C temperature holding for 1 h, the preparation of PA6/TiO_2 composite powders was carried out.

3.3. Evaluation of LPBF processability of composite powder

Based on the precipitation process of PA6 powder, the PA6/TiO_2 composite powders are prepared. As a polymer material, PA6 provides a carbon source for the carbonization preparation of C-TiO_2 photocatalytic material. Carbon-complexed TiO_2 can increase the efficiency of photogenerated carrier separation, and the photogenerated carrier electrons are transferred to C. Therefore, the combination probability of electrons and holes will be greatly reduced, and the photocatalytic efficiency of TiO_2 will be improved. The preparation process of PA6 powder directly determines the network morphology of the precipitated PA6/TiO_2 composite powder, which, further, determines the network morphology of C-TiO_2. In this section, based on the preparation process of pure PA6 powder, porous PA6/TiO_2 composite powders were prepared and the HT-LPBF processability was evaluated.

Figure 8 shows the TEM images and SEAD pattern of the P25-type TiO_2, which is a highly dispersed gas-phase nano-TiO_2. It can be observed from the TEM images that TiO_2 is composed of a large number of nanoscale particles with a size of ~20 nm. HRTEM image shows that the sample is composed of a clear lattice. The interplanar spacing is 3.581 Å, corresponding to the (0 1 0) crystal plane of anatase TiO_2. It can also be observed from the SAED pattern in Figure 8D that there are diffraction rings of 1 0 1, 0 0 4, 2 0 0, and 1 0 5 planes of anatase TiO_2 and those of 2 1 1, 1 1 0, and 1 1 1 planes of rutile phase. Therefore, it can be concluded that the TiO_2 contains a mixed phase of rutile and anatase phases. This can also be proven by XRD analysis (Figure 9). Meanwhile, with the increase of TiO_2 content in the composite powders, the diffraction intensity of TiO_2 was enhanced. The diffraction angle of TiO_2 in the composite powder was shifted to a low 2θ, indicating an increase in the interplanar spacing. This may be attributed to the intercalation of TiO_2 by PA6 molecules under a high-temperature and high-pressure solution environment.

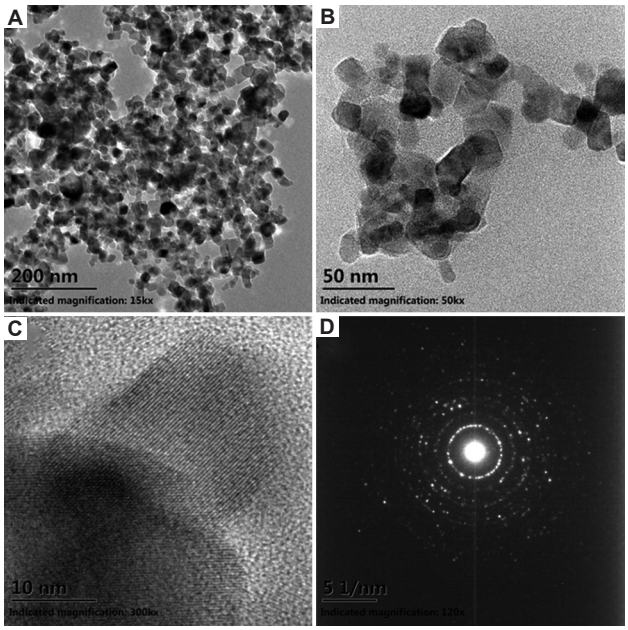

Figure 8. (A and B) TEM images of P25-type TiO_2. (C) HRTEM image. (D) SAED diffraction pattern. SEAD: Selected area electron diffraction.

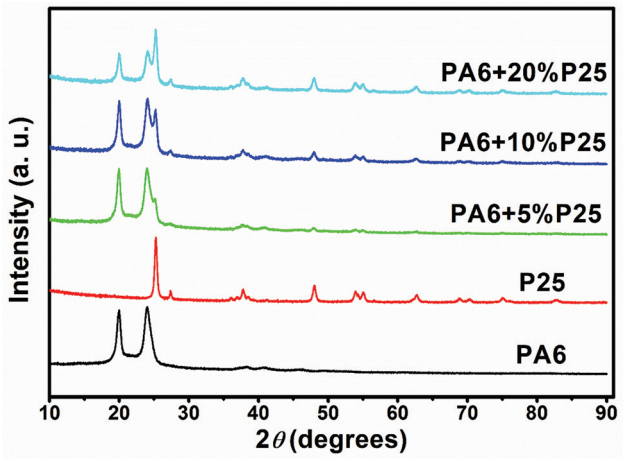

Figure 9. XRD diffraction curves of PA6, P25-type TiO_2, and their composites.

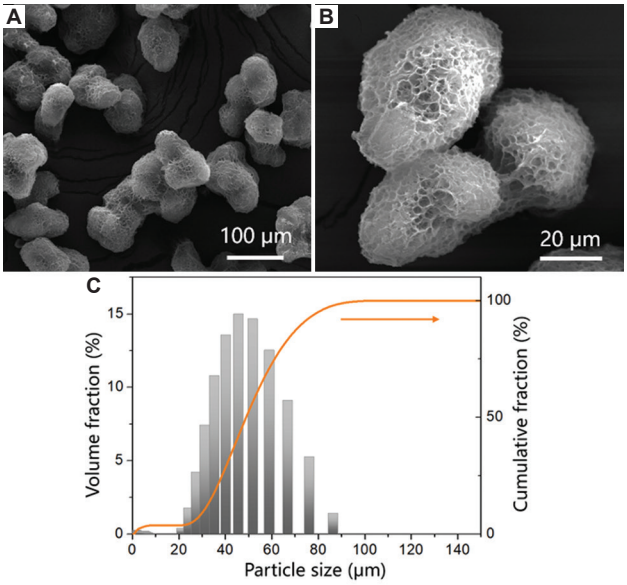

Figure 10. (A and B) Typical microstructure of PA6/TiO_2 composite powder and (C) its particle size distribution.

As shown in Figures 10 and 11, the PA6/TiO_2 composite powders were near-spherical, and there was a weak inter-bonding between the particles. The surface of the powder showed an obvious microporous structure, on which TiO_2 was evenly distributed, and the specific surface area of the powder reached 240.5 m^2/kg. Due to the generation of the porous network morphology, the bulk density of the powder decreased, as shown in Table 2, especially for the composite powders. On the one hand, this may cause large shrinkage during the LPBF process, which is not conducive to the control of part accuracy. On the other hand, this is very beneficial to the uniform absorption of incident light and the improvement of photocatalytic efficiency.

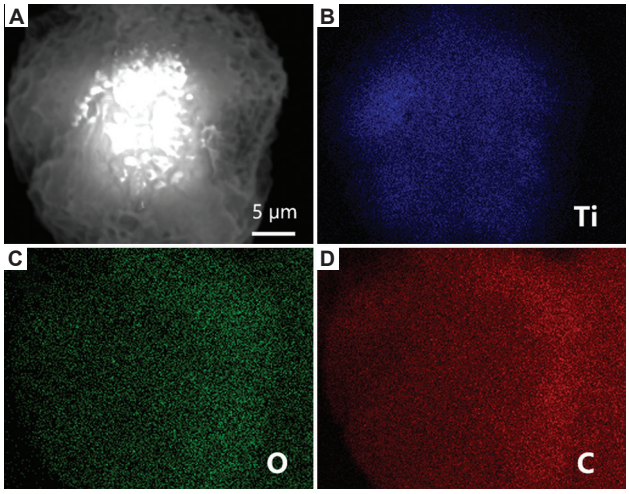

Figure 11. EPMA-WDS element mapping of composite powder shows the distribution of TiO_2 in particle. (A) Microstructure of composite powder, (B) Ti, (C) O, and (D) C element distribution. EPMA-WDS: Electron probe microanalyzer-wavelength dispersive spectrometer.

Laser particle size testing showed that the composite powder exhibited a good normal distribution, although there were some small particles below 10 μm. The Dv(10), Dv(50), and Dv(90) of the composite powder were 31 μm, 48.8 μm, and 72.6 μm, respectively. The AOR values of the prepared PA6 and its TiO_2 composite powders are at or below 30°, indicating good powder flowability and spreading properties compared with LPBF-graded PA12 and PEEK powders[25,26]. Therefore, from the perspective of powder flowability and particle size distribution, the prepared PA6/TiO_2 composite powder is suitable for the LPBF process[27,28].

In addition, from the perspective of rheology properties, the studies demonstrated that PA6 has a similar melt flow index to that of the commercial LPBF-graded PA12 material, indicating suitable melt processing properties of PA6[29,30]. As the DPPC process does not change the essential macromolecular structure of the raw material, it can, therefore, be expected that the rheology properties of the prepared powders are suitable for the LPBF process. From the perspective of thermal properties, the sintering window of the composite powder is broadened from 19.7°C to 26.6°C compared to pure PA6, showing better processability (Figure 12)[31,32]. With the increase of the initial melting and crystallization temperatures of the composite powder, higher powder bed temperature and slower cooling control are required to obtain better mechanical properties and dimensional accuracy.

In general, the PA6/TiO_2 composite powder prepared by the DPPC method has great potential to be used for the LPBF process to fabricate 3D photocatalytic material with a characteristic macro-micro porous structure.

Table 2. Properties of PA6 and its TiO_2 composite powders

Parameter	PA6 (125°C, 1 h, 50 g/L)	PA6 (125°C, 1 h, 150 g/L)	PA6/5% TiO_2	PA6/10% TiO_2	PA6/20% TiO_2
Bulk density (g/cm^3)	0.36±0.001	0.31±0.002	0.28±0.006	0.28±0.004	0.26±0.002
Angle of repose (°)	30.39±0.29	30.75±0.45	29.77±0.68	26.62±0.5	25.96±0.73

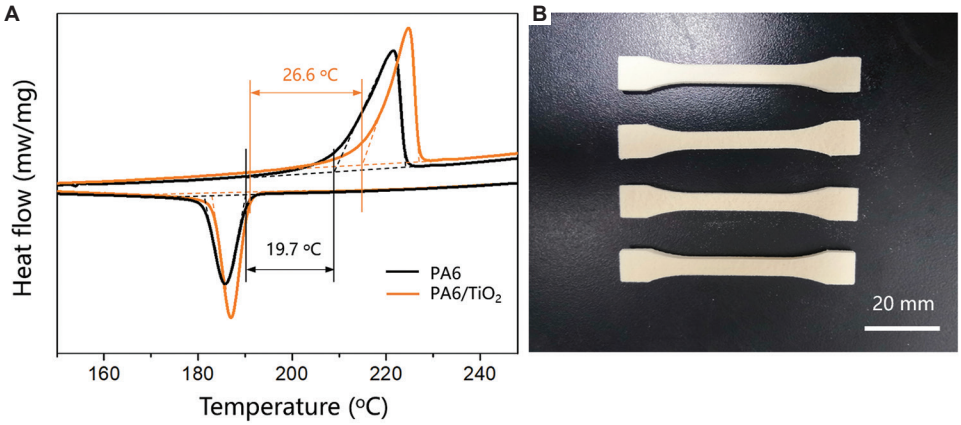

Figure 12. (A) Comparison of DSC curves between PA6 and its TiO_2 composite powders indicating the changes in LPBF processability, and (B) the printed PA6 samples proving the LPBF processability.

4. Conclusion

In this study, the PA6/TiO_2 photocatalytic composite was prepared based on DPPC method, and its LPBF processability was investigated. The main conclusions are as follows:

(i) Holding the crystallization precipitation temperature at 125°C for 1 h, nearly spherical PA6 powders with a particle size of 20–90 μm and a normal distribution peak of 49.3 μm can be obtained.
(ii) Increasing the dissolved concentration of PA6 to 150 g/L will increase the temperature gradient of the reactor, resulting in a porous-surfaced powder and a wide particle size distribution.
(iii) PA6/TiO_2 composite powder has a characteristic spherical porous-surfaced morphology, a high specific surface area of 240.5 m^2/kg, an appropriate Dv(50) of 48.8 μm, and a wide sintering window of 26.6°C, which make it suitable for LPBF process and improvement of photocatalytic efficiency.

This paper describes the preparation of a PA6/TiO_2 powder material for LPBF additive manufacturing of photocatalytic composites and also presents a novel idea for the preparation of macro-micro 3D network TiO_2-based photocatalytic composites.

Acknowledgments

The authors would also like to thank the State Key Laboratory of Materials Processing and Die and Mould Technology and the HUST Testing Center.

Funding

The study was supported by National Natural Science Foundation of China (52105341), China Postdoctoral Science Foundation (2020M682406), Post-Doctoral Innovative Research Post of Hubei Province (Post-doc No. 257963), Fundamental Research Funds for the Central Universities (2019kfyRCPY044 and 2021GCRC002), Program for HUST Academic Frontier Youth Team (2018QYTD04), and Guangdong Provincial Enterprise Key Laboratory for 3D Printing Polymer and Composite Materials (2018B030323001).

Conflict of interest

The authors declare that they have no known competing financial interests or personal relationships that could have appeared to influence the work reported in this paper.

Author contributions

Conceptualization: Peng Chen, Chunze Yan
Data curation: Zhaoqing Li, Haoze Wang
Formal analysis: Zhaoqing Li, Jin Su
Funding acquisition: Chunze Yan, Yusheng Shi
Investigation: Sheng Liu, Haoze Wang
Methodology: Peng Chen
Supervision: Chunze Yan, Yusheng Shi
Validation: Sheng Liu, Jin Su
Writing – original draft: Peng Chen
Writing – review & editing: Peng Chen, Lei Yang, Chunze Yan

References

1. Chen XB, Liu L, Huang FQ, 2015, Black titanium dioxide (Ti_{O2}) nanomaterials. *Chem Soc Rev*, 44: 1861–1885.

   https://doi.org/10.1039/c4cs00330f

2. Hu X, Hu XJ, Peng QQ, *et al.*, 2020, Mechanisms underlying the photocatalytic degradation pathway of ciprofloxacin with heterogeneous TiO_2. *Chem Eng J*, 380: 122366.

   https://doi.org/10.1016/j.cej.2019.122366

3. Wang D, Zhi T, Liu LH, *et al.*, 2022, 3D printing of TiO_2 nano particles containing macrostructures for As(III) removal in water. *Sci Total Environ*, 815: 152754.

   https://doi.org/10.1016/j.scitotenv.2021.152754

4. Kamrannejad MM, Hasanzadeh A, Nosoudi N, *et al.*, 2014, Photocatalytic degradation of polypropylene/TiO_2 nanocomposites. *Mater Res Am J Mater*, 17: 1039–1046.

   https://doi.org/10.1590/1516-1439.267214

5. Li Z, Liu Z, Yang X, *et al.* 2022, Enhanced photocatalysis of black TiO_2/graphene composites synthesized by a facile Sol–Gel method combined with hydrogenation process. *Materials*, 15: 3336.

   https://doi.org/10.3390/ma15093336

6. Shuai C, Shuai C, Feng P, *et al.*, 2018, Antibacterial capability, physicochemical properties, and biocompatibility of $nTiO_{(2)}$ incorporated polymeric scaffolds. *Polymers* (*Basel*), 10: 328.

   https://doi.org/10.3390/polym10030328

7. Kayaci F, Vempati S, Ozgit-Akgun C, *et al.*, 2014, Selective isolation of the electron or hole in photocatalysis: ZnO-TiO_2 and TiO_2-ZnO core-shell structured heterojunction nanofibers via electrospinning and atomic layer deposition. *Nanoscale*, 6: 5735–5745.

   https://doi.org/10.1039/c3nr06665g

8. Xu XY, Wang M, Lin L, *et al.*, 2015, Efficient visible-light photocatalysts from sensitized TiO_2 nanospheres. *Mater Sci Forum*, 814: 31–38.

   https://doi.org/10.4028/www.scientific.net/msf.814.31

9. Shuang S, Lv R, Xie Z, *et al.*, 2016, Surface plasmon enhanced photocatalysis of Au/Pt-decorated TiO_2 nanopillar arrays. *Sci Rep*, 6: 26670.

   https://doi.org/10.1038/srep26670

10. Wang DH, Jia L, Wu XL, *et al.*, 2012, One-step hydrothermal synthesis of N-doped TiO2/C nanocomposites with high visible light photocatalytic activity. *Nanoscale*, 4: 576–584.

    https://doi.org/10.1039/c1nr11353d

11. Wang Q, Zhang LX, Guo YK, *et al.*, 2020, Multifunctional 2D porous g-C3N4 nanosheets hybridized with 3D hierarchical TiO_2 microflowers for selective dye adsorption, antibiotic degradation and CO_2 reduction. *Chem Eng J*, 396: 125347.

    https://doi.org/10.1016/j.cej.2020.125347

12. Carp O, Huisman CL, Reller A, 2004, Photoinduced reactivity of titanium dioxide. *Prog Solid State Chem*, 32: 33–177.

    https://doi.org/10.1016/j.progsolidstchem.2004.08.001

13. Fattakhova-Rohlfing D, Zaleska A, Bein T, 2014, Three-dimensional titanium dioxide nanomaterials. *Chem Rev*, 114: 9487–9558.

    https://doi.org/10.1021/cr500201c

14. Yang L, Yan C, Fan H, *et al.*, 2019, Investigation on the orientation dependence of elastic response in Gyroid cellular structures. *J Mech Behav Biomed Mater*, 90: 73–85.

    https://doi.org/10.1016/j.jmbbm.2018.09.042

15. Yang L, Yan C, Han C, *et al.*, 2018, Mechanical response of a triply periodic minimal surface cellular structures manufactured by selective laser melting. *Int J Mech Sci*, 148: 149–157.

    https://doi.org/10.1016/j.ijmecsci.2018.08.039

16. Skorski MR, Esenther JM, Ahmed Z, *et al.*, 2016, The chemical, mechanical, and physical properties of 3D printed materials composed of TiO_2-ABS nanocomposites. *Sci Technol Adv Mater*, 17: 89–97.

    https://doi.org/10.1080/14686996.2016.1152879

17. Chen P, Su J, Wang H, *et al.*, 2022, Mechanical properties and microstructure characteristics of lattice-surfaced PEEK cage fabricated by high-temperature laser powder bed fusion. *J Mater Sci Technol*, 125: 105–117.

    https://doi.org/10.1016/j.jmst.2022.03.009

18. Chen P, Wang H, Su J, *et al.*, 2022, Recent advances on high-performance polyaryletherketone materials for additive manufacturing. *Adv Mater*, 2200750.

    https://doi.org/10.1002/adma.202200750

19. Yang L, Wu S, Yan C, *et al.*, 2021, Fatigue properties of Ti-6Al-4V Gyroid graded lattice structures fabricated by laser powder bed fusion with lateral loading. *Addit Manuf*, 46: 102214.

    https://doi.org/10.1016/j.addma.2021.102214

20. Wu S, Yang L, Wang C, *et al.*, 2022, Ceramic lattices with a triply periodic minimal surface structure prepared by laser powder bed fusion. *Addit Manuf*, 56: 102910.

    https://doi.org/10.1016/j.addma.2022.102910

21. Hussein A, Hao L, Yan C, *et al.*, 2013, Young, advanced lattice support structures for metal additive manufacturing. *J Mater Process Tech*, 213:1019–1026.

    https://doi.org/10.1016/j.jmatprotec.2013.01.020

22. Yan C, Hao L, Hussein A, *et al.*, 2012, Evaluations of cellular lattice structures manufactured using selective laser melting. *Int J Machine Tools Manuf*, 62: 32–38.

https://doi.org/10.1016/j.ijmachtools.2012.06.002

23. Chen P, Wu H, Zhu W, *et al*., 2018, Investigation into the processability, recyclability and crystalline structure of selective laser sintered polyamide 6 in comparison with polyamide 12. *Polym Test*, 69: 366–374.

    https://doi.org/10.1016/j.polymertesting.2018.05.045

24. Chen B, Berretta S, Davies R, *et al*., 2019, Characterisation of carbon fibre (Cf) Poly Ether Ketone (PEK) composite powders for laser sintering. *Polym Test*, 76: 65–72.

    https://doi.org/10.1016/j.polymertesting.2019.03.011

25. Chen B, Wang Y, Berretta S, *et al*., 2017, Poly aryl ether ketones (PAEKs) and carbon-reinforced PAEK powders for laser sintering. *J Mater Sci*, 52: 6004–6019.

    https://doi.org/10.1007/s10853-017-0840-0

26. Berretta S, Ghita O, Evans KE, 2014, Morphology of polymeric powders in laser sintering (LS): From polyamide to new PEEK powders. *Eur Polym J*, 59: 218–229.

    https://doi.org/10.1016/j.eurpolymj.2014.08.004

27. Chen P, Su J, Wang H, *et al*., 2022, Aging mechanism of polyetheretherketone powder during layer-wise infrared radiation of high-temperature laser powder bed fusion. *Mater Des*, 213: 110348.

    https://doi.org/10.1016/j.matdes.2021.110348

28. Su J, Hua S, Chen A, *et al*., 2021, Three-dimensional printing of gyroid-structured composite bioceramic scaffolds with tuneable degradability. *Mater Sci Eng C*, 133: 112595.

    https://doi.org/10.1016/j.msec.2021.112595

29. Salmoria GV, Leite JL, Vieira LF, *et al*., 2012, Mechanical properties of PA6/PA12 blend specimens prepared by selective laser sintering. *Polym Test*, 31: 411–416.

    https://doi.org/10.1016/j.polymertesting.2011.12.006

30. Salmoria GV, Leite JL, Paggi RA, 2009, The microstructural characterization of PA6/PA12 blend specimens fabricated by selective laser sintering. *Polym Test*, 28: 746–751.

    https://doi.org/10.1016/j.polymertesting.2009.06.010

31. Wang H, Chen P, Wu H, *et al*., 2022, Comparative evaluation of printability and compression properties of poly-ether-ether-ketone triply periodic minimal surface scaffolds fabricated by laser powder bed fusion. *Addit Manuf*, 57: 102961.

    https://doi.org/10.1016/j.addma.2022.102961

32. Guo B, Xu Z, Luo X, *et al*., 2021, A detailed evaluation of surface, thermal, and flammable properties of polyamide 12/glass beads composites fabricated by multi jet fusion. *Virtual Phys Prototy*, 16: S39–S52.

    https://doi.org/10.1080/17452759.2021.1899463